Draft Version April 19, 2018
Preprint typeset using LaTeX style emulateapj v. 12/16/11

PLANCK CLUSTER PAPER

SB[1], JPH[1], FM, PD[1]

Draft Version April 19, 2018

ABSTRACT

We propose to continue our program of optical imaging to unveil all of the most massive clusters in the observable Universe. We start from the all-sky Planck Sunyaev-Zeldovich (SZ) catalogs, which contain several hundred high significance (signal-to-noise ratio, SNR > 5) unconfirmed cluster candidates. Since SZ selection favors high mass clusters and the Planck confirmation process favored low redshift systems, the highest significance unconfirmed candidates are, therefore, likely massive clusters ($M_{500} > 5 \times 10^{14}$ M$_\odot$) at relatively high redshift ($z > 0.5$). Our proposed observations, using MOSAIC-3 on Mayall, are designed to confirm the presence of a brightest cluster galaxy (to $z \sim 1$) and red sequence of accompanying cluster members (to $z \sim 0.7$). Preliminary results from our observations over the past two years have validated our approach by the detection of optical clusters in a number of Planck candidates, including the discovery of rich systems at $z = 0.553$ and $z = 0.830$ that rival the most massive clusters known. The proposed observations represent the first step required to provide a complete all-sky census throughout the observable Universe of the most massive, high redshift clusters. Their expected high redshift and high mass make the unconfirmed Planck clusters, arguably, the most important available sample for probing deviations from ΛCDM and defining the high-mass end of the cluster mass function.
Subject headings:

1. INTRODUCTION

this section has not been edited and is just a bunch of stuff copy and pasted. I did update some of the references. Massive galaxy clusters at high redshifts are rare beasts that hold important clues to the evolution of structure in the Universe and in principle can help probe (or falsify) structure formation models under the ΛCDM paradigm (e.g., Mortonson et al. 2011; Harrison & Coles 2012; Harrison & Hotchkiss 2012; Waizmann et al. 2012; Zitrin et al. 2009). Galaxy clusters also harbor a significant fraction of the visible baryons in the Universe, in the form of a hot intracluster medium that leaves an imprint on the Cosmic Microwave Background (CMB) though the Sunyaev-Zel'dovich (SZ; Sunyaev & Zeldovich 1972 effect.

The surface brightness of the SZ effect does not depend on redshift, therefore providing uniform samples of massive clusters up to arbitrary distances. This has been borne out by the large area surveys of the Atacama Cosmology Telescope (ACT; Swetz et al. 2011) and the South Pole Telescope (SPT; Carlstrom et al. 2011 that have detected hundreds of massive clusters since 2008 up to redshifts of $z \sim 1.4$ (see Reichardt et al. 2013 and Hasselfield et al. 2013 for latest results). Now, Planck has released an all-sky SZ sample (PSZ; Planck Collaboration et al. 2014) that contains 861 confirmed clusters (of which most [683] were known previously) and another 366 unconfirmed cluster candidates.

We led the ACT cluster confirmation process using 4-m class telescopes; now we propose to use our well-established expertise to identify Planck clusters. The recent SZ cluster samples have opened a new window into extreme systems, the most massive clusters at high redshift (Foley et al. 2011; Menanteau et al. 2012), prompting studies that match their observed numbers with the abundance predictions of ΛCDM cosmology (Hoyle et al. 2011, Mortonson et al. 2011, Waizmann et al. 2012). There are few, if any, clusters at high redshift ($z > 0.8$) and high mass ($M_{200} > 10^{15}$ M$_\odot$) in the cosmological simulations (see Tinker et al. 2008), so the halo mass function at high-z and high-M is essentially unconstrained. Thus, with the proposed observations we will determine the abundance of massive clusters at high redshift making a direct observational measurement of the high-z, high-M end of the halo mass function. For example, one of the most impressive results of the ACT SZ survey is our discovery of the high redshift ($z = 0.87$), extreme cluster "El Gordo" (ACT-CL J0102-4915), the most significant SZ detection of the whole survey (and also of the SPT survey). Our recent HST weak-lensing analysis has provided an independent mass estimation $M_{200a} = (3.1 \pm 0.7) \times 10^{15}$ M$_\odot$ (Jee et al. 2013) that confirms our earlier mass estimates for the cluster (Menanteau et al. 2012). Based on its estimated mass alone, "El Gordo" is a very rare system within the ACT+SPT (2800 sq. deg.) survey area, but is still consistent with the expectations of ΛCDM. We are now at a unique moment in cluster science where we can discover all massive clusters in the observable universe. This census will measure the high-mass, high-redshift cluster mass function, and determine the extent of deviations from the theoretical halo mass function (Jenkins et al. 2001; Tinker et al. 2008).

Assuming WMAP7 cosmology (Komatsu et al. 2011) with the Tinker et al. (2008) halo mass function, there should be only $\sim$ 4 clusters as massive as El Gordo ($\leq 2 \times 10^{15}$ M$_\odot$) at $z > 0.6$ in the full area covered by the Planck PSZ catalog (83.7% of the sky). Although Plancks larger beam size (compared to both ACT and SPT) makes it more sensitive to clusters at lower red-

[1] Rutgers;boada@physics.tamu.edu

shifts (due to their larger projected area on the sky), among the 861 confirmed clusters in the recently released all-sky Planck SZ catalog are the two highest significance high-redshift SZ detections from ACT (as well as several other ACT and SPT clusters). This confirms the ability of Planck to unambiguously detect the most massive clusters at high redshift. In fact Planck reports "El Gordo" ($z = 0.87$) and ACT-CL J2327.40204 ($z = 0.701$) at S/N values of 8.0 and 6.3, respectively. And as Figure 2 (right panel) shows, these are the two most massive Planck clusters in the confirmed sample at high redshift. For the new clusters we confirm, our experimental design allows us to estimate photometric redshifts, which will be sufficiently accurate for a meaningful estimate of the clusters mass from the Planck SZ signal.

Unless otherwise noted, throughout this paper, we use a concordance cosmological model ($\Omega_\Lambda = 0.7$, $\Omega_m = 0.3$, and $H_0 = 70$ km s^{-1}Mpc^{-1}), assume a Chabrier initial mass function (Chabrier 2003), and use AB magnitudes (Oke 1974).

2. DESIGN

Among the recently released, second, all-sky PSZ catalog[2] (hereafter PSZ2; Planck Collaboration et al. 2015) there are 450 unconfirmed SZ detections with S/N > 4.5. The vast majority of these must lie at high-z because the Planck confirmation process mostly relied on existing catalogs with a preference for low-z clusters. Furthermore, the confirmed sample has a small fraction (3%) of $z > 0.6$ clusters compared to that expected ($\sim$ 20%) based on the theoretical halo mass function (Jenkins et al. 2001; Tinker et al. 2008). If other clusters like "El Gordo" exist, they are hiding as high-significance candidates within the objects in this catalog. The design of the observations is to use both optical and near-infrared (NIR) imaging to confirm the SZ detections as real clusters and provide photometric redshifts using the multi-color information.

Our strategy is to use the Kitt Peak National Observatory (KPNO) Mayall-4m telescope imaging as the first and fundamental step to confirm the highest significance detections in the PSZ2 catalog that are visible across the entire northern sky. Following closely the procedure used for ACT follow-up citation?, targets are prioritized by SZ signal-to-noise (S/N). We choose to initially report on targets with PSZ2 S/N > 5 as the statistical reliability of PSZ2 cluster candidates is quite high: according to the Planck team $\sim$ 90% of candidates at S/N > 5 turn out to be "real" clusters (citation? maybe show the figure from the proposal).

Optical imaging will be sufficient to confirm nearly all of the candidates, but for the highest redshift ones, NIR data will be necessary. Again following the procedure for ACT cluster follow-up: those candidates with some evidence for a high-z brightest cluster galaxy (BCG; note that we can detect BCGs to $z \sim 1.5$) will be targeted with NIR observations to confirm the presence of a BCG and detect the red sequence of cluster members. Observational priority again is given to higher S/N candidates.

2.1. *Observations*

All observations were conducted with the KPNO Mayall telescope. The optical observations were made with the MOSAIC camera mounted at the prime focus. Two detector packages were used for the observations. The earlier MOSAIC1.1 instrument consisted of eight 2048 × 4096 SITe CCDs, arranged 2 × 4, separated by a $\sim$ 50 pixels gap with a pixel scale of 0.″26 pixel^{-1}. MOSAIC1.1 was replaced with Mosaic3, in year?, and consists of four new 4k×4k, 15 micron pixel, 500-micron thick LBNL deep-depletion CCDs. Because the only change from MOSAIC1.1 to MOSAIC3 are the CCDs and controllers both versions have a 36′ × 36′ field-of-view.

need to talk about the dithering

The optical observing strategy consists of targeted *griz* observations of individual candidates with exposure times of 350 s, 350 s, 1100 s and 1100 s (assuming dark conditions) to provide 5σ detections limits of g =??, $r = 24.5$, $i = 24.5$, $z = 24.2$ ensuring the unambiguous detection of the faint (i.e., 0.4L$\star$) galaxies in the red cluster sequence up to $z \sim 1.0$ (citation?) and of brightest cluster galaxies (BCGs) to higher redshifts. The choice of filters in our program is driven by the need to segregate early-type galaxies in the cluster through their colors (or photometric redshifts) by sampling blueward and red-ward of the 4000Å break. Our depths are quite a bit different that the designed depths. Should we mention that here, or wait till later on when we are discussing how we actually did?

TABLE 1 Basic properties of the galaxy clusters candidates targeted for observation with the MOSAIC and NEWFIRM instruments: Column 1: Cluster name; Column 2: The right ascension of the cluster; Column 3: The declination of the cluster; Column 4: the PSZ1 catalog S/N ratio; Column 5: the PSZ2 catalog S/N ratio; Column 6: The date of MOSAIC observations

Cluster (1)	RA (J2000) (2)	DEC (J2000) (3)	PSZ1 SNR (4)	PSZ2 SNR (5)	MOSAIC Obs. (6)
PSZ1 G031.91+67.94	14:29:02	+24:37:33.38	5.23	nan	Feb, 2014
PSZ1 G055.83-41.64	21:57:14	-2:31:51	5.72	nan	Oct, 2014
PSZ1 G084.62-15.86	21:49:44	+33:10:23.81	6.01	nan	Oct, 2014
PSZ1 G096.44-10.40	22:19:35	+44:31:05.27	6.55	nan	Oct, 2014
PSZ1 G102.86-31.07	23:33:08	+28:43:51.60	6.12	nan	Oct, 2014
PSZ1 G102.97-04.77	22:34:47	+52:43:13.90	5.64	nan	Oct, 2014
PSZ1 G105.91-38.39	23:53:54	+22:34:21.09	7.16	nan	Oct, 2014
PSZ1 G108.90-52.04	0:16:38	+09:52:49.98	6.89	nan	Jun, 2017
PSZ1 G118.06+31.10	15:54:34	+84:10:37.49	6.00	nan	Feb, 2014
PSZ1 G127.55+20.84	3:10:51	+82:25:43.91	5.91	nan	Oct, 2014
PSZ1 G138.60-10.85	2:27:02	+49:04:54.07	8.26	nan	Oct, 2014
PSZ1 G142.17+37.28	9:18:56	+70:52:01.14	5.79	nan	Feb, 2014
PSZ1 G142.38+22.82	6:13:40	+71:52:21.02	5.82	nan	Feb, 2014
PSZ1 G146.00-49.42	1:51:35	+10:44:02.79	6.62	nan	Oct, 2014

TABLE 1 Continued

Cluster	RA (J2000)	DEC (J2000)	PSZ1 SNR	PSZ2 SNR	MOSAIC Obs.
(1)	(2)	(3)	(4)	(5)	(6)
PSZ1 G148.20+23.49	6:37:46	+66:54:24.40	8.40	nan	Feb, 2014
PSZ1 G153.41+36.58	8:42:40	+62:34:31.61	6.85	nan	Feb, 2014
PSZ1 G153.56+36.23	8:39:31	+62:31:30.58	5.96	nan	Feb, 2014
PSZ1 G162.30-26.92	3:24:26	+24:00:44.46	6.56	nan	Oct, 2014
PSZ1 G169.80+26.10	7:30:08	+48:20:02.06	5.32	nan	Oct, 2014
PSZ1 G183.26+12.25	6:42:56	+31:49:07.58	5.43	nan	Oct, 2014
PSZ1 G185.93-31.21	4:11:39	+06:16:00.67	5.90	nan	Jan, 2014
PSZ1 G206.45+13.89	7:29:59	+11:56:22.64	5.90	nan	Feb, 2014
PSZ1 G224.82+13.62	8:01:42	-4:03:54	5.51	nan	Jan, 2014
PSZ1 G249.01+73.75	11:56:46	+16:55:43.68	7.14	nan	Feb, 2014
PSZ1 G286.25+62.68	12:21:10	+00:47:34.05	5.52	nan	Feb, 2014
PSZ1 G341.69+50.66	14:25:20	-4:59:54	5.48	nan	Feb, 2014
PSZ2 G022.03+17.75	17:28:37	-1:13:03	5.64	6.20	Jun, 2017
PSZ2 G023.05+20.52	17:20:47	+00:58:06.58	nan	5.57	Jun, 2017
PSZ2 G024.46-18.08	19:42:23	-15:26:09	nan	6.98	Jun, 2017
PSZ2 G027.77+10.88	18:03:22	+00:25:57.59	nan	6.42	Jun, 2016
PSZ2 G028.15-08.62	19:13:41	-8:08:26	5.07	7.67	Jun, 2017
PSZ2 G029.66-47.63	21:45:44	-21:46:49	nan	5.74	Nov, 2016
PSZ2 G029.80-17.40	19:48:32	-10:31:40	6.59	9.01	Jun, 2016
PSZ2 G031.41-19.16	19:57:41	-9:53:56	4.60	5.69	Jun, 2017
PSZ2 G032.12-14.96	19:43:34	-7:27:45	8.21	9.12	Jun, 2017
PSZ2 G033.27-17.54	19:54:52	-7:36:11	5.78	6.86	Jun, 2017
PSZ2 G036.69-15.67	19:54:05	-3:50:23	nan	5.69	Jun, 2017
PSZ2 G043.44-41.27	21:36:44	-10:17:48	nan	5.55	Jun, 2017
PSZ2 G044.83+10.02	18:36:39	+15:04:49.72	7.27	9.27	Oct, 2015
PSZ2 G045.50-08.62	19:45:25	+07:04:29.08	4.57	5.63	Jun, 2017
PSZ2 G047.53+08.55	18:46:59	+16:50:35.39	5.82	6.55	Jun, 2016
PSZ2 G048.47+34.86	17:02:08	+27:08:48.05	nan	5.74	Jun, 2016
PSZ2 G065.35-08.01	20:26:04	+24:08:06.72	nan	5.83	Jun, 2016
PSZ2 G071.67-42.76	22:30:54	+05:42:05.22	8.82	8.63	Oct, 2014
PSZ2 G075.08+19.83	18:46:48	+45:46:33.27	nan	5.74	Jun, 2016
PSZ2 G089.06-11.79	21:52:53	+39:03:52.50	nan	5.72	Nov, 2016
PSZ2 G092.11-33.73	23:01:37	+22:28:59.71	nan	5.81	Nov, 2016
PSZ2 G092.46-35.22	23:05:50	+21:19:27.96	5.47	6.73	Oct, 2014
PSZ2 G093.04-32.38	23:01:43	+24:02:24.90	5.69	6.03	Oct, 2014
PSZ2 G096.43-20.89	22:48:09	+35:33:21.47	nan	5.81	Jun, 2016
PSZ2 G098.38+77.22	13:18:25	+38:35:06.94	4.71	5.51	Jun, 2017
PSZ2 G100.22+33.81	17:13:41	+69:22:24.33	nan	5.69	Jun, 2017
PSZ2 G100.45+16.79	20:18:34	+66:47:07.85	nan	11.79	Oct, 2015
PSZ2 G104.15-38.85	23:48:48	+21:43:24.60	nan	6.41	Jun, 2016
PSZ2 G106.11+24.11	19:21:24	+74:33:21.87	nan	5.70	Jun, 2017
PSZ2 G107.41-09.57	23:13:47	+50:19:32.01	nan	10.69	Jun, 2016
PSZ2 G107.83-45.45	0:07:35	+16:07:51.05	nan	7.09	Nov, 2016
PSZ2 G112.07-39.86	0:15:30	+22:14:43.50	nan	5.72	Nov, 2016
PSZ2 G120.76+44.14	13:12:39	+72:53:23.47	nan	5.59	Jun, 2017
PSZ2 G123.35+25.39	1:41:20	+88:13:14.57	5.90	10.86	Oct, 2014
PSZ2 G123.84+25.75	2:55:30	+88:24:01.91	5.04	5.81	Nov, 2016
PSZ2 G125.55+32.72	11:25:35	+83:57:29.12	nan	6.49	Nov, 2016
PSZ2 G127.35-10.69	1:19:42	+51:56:15.39	5.58	6.94	Oct, 2014
PSZ2 G136.31+54.67	11:47:50	+60:45:56.07	nan	6.92	Jun, 2017
PSZ2 G137.24+53.93	11:41:07	+61:11:39.02	nan	7.87	Nov, 2016
PSZ2 G137.58+53.88	11:39:27	+61:09:01.04	5.73	8.18	Feb, 2014
PSZ2 G145.25+50.84	10:53:26	+60:51:43.24	nan	5.98	Jun, 2017
PSZ2 G146.88+17.13	5:34:10	+65:43:14.28	nan	6.13	Nov, 2016
PSZ2 G153.56+36.82	8:44:32	+62:24:41.96	nan	15.90	Nov, 2016
PSZ2 G153.68+36.96	8:45:33	+62:17:12.13	nan	5.07	Nov, 2016
PSZ2 G163.22-26.48	3:28:29	+23:50:15.15	nan	6.35	Nov, 2016
PSZ2 G165.39+09.22	5:47:59	+46:08:39.24	nan	5.60	Nov, 2016
PSZ2 G166.27-24.71	3:42:39	+23:24:41.39	nan	9.58	Nov, 2016
PSZ2 G166.27-25.02	3:41:44	+23:11:00.45	nan	8.09	Nov, 2016
PSZ2 G167.44-38.06	3:09:12	+12:37:11.49	6.11	7.66	Oct, 2014
PSZ2 G171.79-42.08	3:08:40	+07:24:32.96	nan	5.84	Nov, 2016
PSZ2 G173.76+22.92	7:17:28	+44:03:27.62	nan	5.80	Nov, 2016
PSZ2 G181.88-30.77	4:04:21	+09:16:14.87	nan	9.29	Nov, 2016
PSZ2 G189.79-37.25	3:59:37	+00:07:54.80	6.99	7.28	Oct, 2014
PSZ2 G191.82-26.64	4:38:37	+04:42:02.64	4.76	6.17	Nov, 2016
PSZ2 G192.40-67.89	2:18:20	-17:45:23	nan	7.03	Nov, 2016
PSZ2 G194.68-49.76	3:25:22	-9:40:50	5.00	5.71	Nov, 2016
PSZ2 G210.37-37.00	4:32:44	-14:03:01	nan	9.84	Nov, 2016
PSZ2 G210.71+63.08	10:51:42	+24:58:09.19	nan	7.37	Jun, 2017
PSZ2 G210.78-36.25	4:36:07	-14:02:58	nan	6.32	Nov, 2016
PSZ2 G252.45+73.44	11:58:35	+16:00:18.38	nan	5.57	Jun, 2017
PSZ2 G305.76+44.79	12:59:54	-18:01:59	4.72	5.72	Jun, 2017
PSZ2 G310.81+83.91	12:55:01	+21:05:41.16	nan	8.29	Nov, 2016
PSZ2 G318.46+83.79	12:58:33	+21:08:11.93	6.93	9.40	Feb, 2014
PSZ2 G320.94+83.69	12:59:47	+21:06:56.63	nan	7.32	Jun, 2017
PSZ2 G328.96+71.97	13:23:13	+10:43:41.59	nan	5.85	Jun, 2017

TABLE 1 Continued

Cluster	RA (J2000)	DEC (J2000)	PSZ1 SNR	PSZ2 SNR	MOSAIC Obs.
(1)	(2)	(3)	(4)	(5)	(6)

A summary of our observations is given in Table 1.

3. DATA REDUCTION AND CALIBRATION

Standard image reductions including subtraction of dark frames, flat fielding, sky-subtraction, and bad pixel masking was performed by the NOAO virtual observatory using the MOSAIC (Valdes & Swaters 2007) science pipelines. The resultant FITS files consist of fully reduced images with either all single exposure CCDs mosaicked into a single image extension (as in the case of Mosaic1.1) or as a multi-extension FITS file with each single exposure CCD occupying a separate extension.

We then mosaic each separate exposure into a master mosaic as described in the following section.

3.1. *Mosaicking*

Combined mosaics are created with SWARP (Bertin et al. 2002). We create three distinct types of mosaics. The individual dither frames are stacked and then median combined to produce the final completed science mosaic. A "detection" is created by combining select science mosaics into a chi2 image using either the i-band and Ks-band or $i-$ and z-band when Ks imaging is not available. Finally we create a set of mosaics use to produce the three color image used for cluster detection. For this we median combine the $griz$ and Ks science mosaics into a "blue" (gr-bands), "green" ($iz-bands$), and "red" (Ks-band) mosaic. All final mosaics have a pixelscale of $0\farcs25$/pix. The final exposure time is calculated as the median exposure time of the combined images, and similarly the final airmass is median of the individual air masses. need to talk about the weight images

The full parameter file used while creating the mosaics is given in Appendix **??**.

3.2. *Astrometric Calibration*

Each of the final science mosaics produced in the previous section are first astrometrically aligned with *Gaia* (Gaia Collaboration et al. 2016a) Data Release 1 (Gaia Collaboration et al. 2016b) using SCAMP (Bertin 2006) as a part of PHOTOMETRYPIPELINE[3] (PP; Mommert & M. 2017).

Sources are extracted from the mosaics with a signal-to-noise ratio (SNR) of at least ten and with a minimum area of at least 12 pixels. The extracted sources are then matched to the *Gaia* data and a new astrometric solution is calculated. Because the initial astrometric solution from the VO is quite accurate, the resultant corrections are much less than $1''$.

3.3. *Photometric Calibration*

After the mosaics have been astrometrically aligned, we use PP to produce a photometric solution. PP calculates a photometric zero-point in each of our observed bands by comparing field stars located throughout the mosaic to known photometry from large-area sky surveys. Because our sources are spread across the entire northern sky, and because we prefer to minimize the number of differences between photometric solutions we are limited to two optical surveys. For the optical data, we first seek photometric data from the *Sloan Digital Sky Survey* (SDSS; York et al. 2000) Data Release 13 (Alam et al. 2015) get a new citation for dr13 this is for dr12. When our target does not lie within the SDSS footprint we utilize the Panoramic Survey Telescope and Rapid Response System (Pan-STARRS; Chambers et al. 2016) Data Release 1 (hereafter PS1; Flewelling et al. 2016). Both surveys provide accurate $griz$ magnitudes and large on-line queriable databases for rapid automated calibration.

Sources are extracted from the combined mosaics with either a $3''$ or $8''$ diameter aperture for optical sources respectively; sources with a SNR$\geq$ 10 are matched to a survey catalog and a photometric zero-point is determined. We use half of the available stars (with accurate catalog photometry) to derive the zero-point resulting in zero-points calculated from approximately $10-500$ stars and with typical uncertainties of give zp errors in the different bands.

Should we talk about the difference between us and SDSS? If so, how should we "sum up" the differences in a simple way?

4. ANALYSIS

Lorem ipsum dolor amet swag copper mug meh tilde, put a bird on it live-edge tattooed kinfolk before they sold out locavore selvage leggings raclette literally bicycle rights. Hot chicken kickstarter mustache vinyl roof party. Wayfarers brooklyn truffaut twee umami, venmo irony. Typewriter viral pop-up, listicle vaporware organic af salvia keytar twee chillwave austin +1 offal blog. La croix dreamcatcher snackwave, try-hard intelligentsia taxidermy messenger bag air plant godard mustache celiac glossier echo park. Photo booth readymade authentic glossier biodiesel snackwave beard hammock sriracha before they sold out edison bulb fixie PBR&B. Man bun pabst kogi, crucifix subway tile af tacos cray tumeric lyft cronut lomo tattooed.

4.1. *Source Extraction and Photometry*

For source extraction and photometry estimation we use Source Extractor (hereafter SExtractor; version 2.19.5; Bertin & Arnouts 1996) run dual image mode with the CHI2 detection image as the detection image. See Section 3.1. See Appendix **??** for a complete parameter listing.

4.2. *Photometric Redshifts*

We determine photometric redshifts (photo-z) from the five-band optical images using Bayesian Photometric Redshifts (BPZ; Benitez 2000; Coe et al. 2006) following the same procedure as in Menanteau et al. (2009).

We assess the effectiveness of our photo-z estimates by comparing with the available spectroscopic redshifts (spec-z) from the SDSS. We use three diagnostics to

[3] https://github.com/mommermi/photometrypipeline

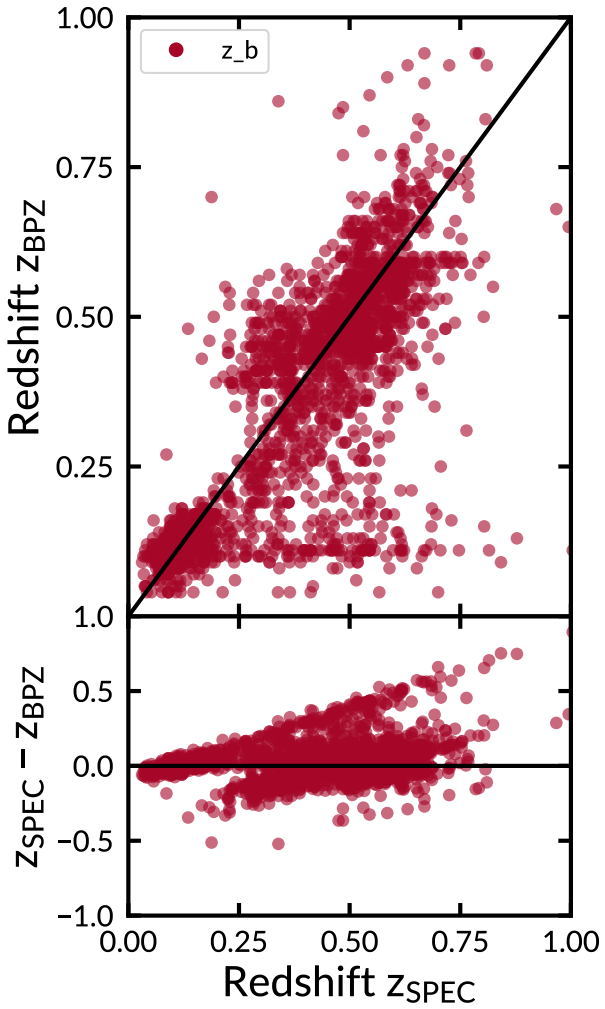

FIG. 1.— Comparison between photometric and spectroscopic redshifts for 2253 galaxies which have spectroscopic redshifts from the SDSS. The photometric redshifts in the top panel use a Bayesian approach with a custom empirical prior on galaxy brightness for the photometric redshifts. The bottom panel shows the difference between the spectroscopic and photometric redshift.

gauge photo-z accuracy. First, we report the full scatter between the photo-z and spec-z, defined as:

$$\sigma_f = \mathrm{RMS}[\delta z/(1+z_{spec})] \quad (1)$$

where $\delta z = z_{spec} - z_{phot}$. Second, we report the normalized median absolute deviation (NMAD; Ilbert et al. 2009; Dahlen et al. 2013; Molino et al. 2017), given as

$$\sigma_{NMAD} = 1.48 \times \mathrm{median}\left(\frac{|\delta z|}{1+z_{spec}}\right). \quad (2)$$

which provides an estimate of the scatter resistant to catastrophic outliers. Finally, the catastrophic outlier fraction (OLF) where we define a catastrophic outlier (following Molino et al. 2017) as,

$$\eta = \frac{|\delta z|}{(1+z_{spec})} > 5 \times \sigma_{NMAD}. \quad (3)$$

Figure 1 shows the photometric redshift performance as a function of the true spectroscopic redshift. For the full sample of galaxies we calculate $\sigma_f = XX\%$, $\sigma_{NMAD} = XX\%$, and an outlier fraction, $\eta = XX\%$. When considering the performance of only the galaxies BPZ classified as E and E/S0 type, we find the following results; $\sigma_f = 10.4\%$, $\sigma_{NMAD} = 5.43\%$, and an outlier fraction, $\eta = 2.97\%$.

4.3. *Cluster Finding*

In this section, we briefly describe the algorithms and methods use to select the galaxy clusters from the multi-wavelength optical imaging. We follow the methods described in detail in Menanteau et al. (2009, 2010a). We direct the reader there for an in depth description and discussion of the methods.

We first create a three-color image using STIFF (Bertin & Emmanuel 2011). The red, green, and blue channels are given by the corresponding combined mosaics described in Section 3.1. We then visually inspect an area of roughly $8' \times 8'$ centered on the position of each unconfirmed cluster; see Table 1. Potential brightest cluster galaxies (BCGs) are identified by first calculating the absolute limiting magnitude needs details.

Once a potential BCG is selected, the algorithm selects nearby galaxies, within $|z_{BCG} - z| < 0.05$ and 0.5 Mpc projected radius, which BPZ has classified as either E or E/S0 galaxies. These photo-z's of the galaxies are combined using a 3σ median sigma-clipping algorithm to estimate the cluster's mean redshift, z_c. We use this mean cluster redshift measurement and the member selection criteria given previously to estimate the number of cluster members within 1 Mpc, $N_{1\mathrm{Mpc}}$, which we define as the richness of the cluster, N_{gal}.

We correct the N_{gal} estimate by subtracting a statistical background of galaxies. We first estimate the number of background ellipticals by selecting galaxies within an annulus ($R_{200} < r < 2R_{200}$) around each cluster's position. We include galaxies with $\delta z = 0.05$ and similar colors as those galaxies assumed to belong to the cluster. These galaxies are subtracted from the cluster's population which provides an corrected N_{gal}, N_{galc}, which we then use to compute other important quantities. In practice the corrected number of galaxies is between 15% and 20% lower than the uncorrected number (Menanteau et al. 2010a). We report N_{galc} for the remainder of this work.

4.4. *Recovery of the Brightest Cluster Galaxies*

We have designed our observations to detect BCGs to $z \sim 1.5$. To quantify the actual depth of our images, we perform a Monte Carlo simulation by injecting artificial sources and computing their recovery fraction. We create the artificial sources with the MODELING package, part of ASTROPY (The Astropy Collaboration et al. 2013).

Following the procedure given in Menanteau et al. (2010b), the synthetic galaxies are created to have de Vaucouleurs (de Vaucouleurs 1948) profiles and surface brightnesses corresponding to their magnitude and assumed sizes. We inject the artificial galaxies into our science images with similar noise characteristics as their real counterparts.

We generate four rounds of one hundred elliptical galaxies spread uniformly across our science imaging. Each round of galaxies are place at different random positions to suppress abnormally boosted recovery fractions

due to source confusion. The artificial galaxies have total fluxes corresponding to apparent magnitudes between 19 mag $< i <$ 27 mag with 0.1 mag spacing.

This is almost directly taken from FM2010 – edit. We use the individual field's completion limit to estimate the redshift to which we can reliably detect massive clusters. For this, we compare the completeness limits of our observations to the expected and observed (i.e., known) apparent magnitudes of galaxies in clusters as a function of redshift. We estimated the expected apparent galaxy i-band magnitude as a function of redshift using $L_\star$ as defined for the population of red galaxies by Blanton et al. (2003) at $z = 0.1$ and allowing passive evolution according to a solar metallicity (Bruzual & Charlot 2003) $\tau = 1.0$ Gyr burst model formed at $zf = 5$. We show this in Figure 2 for a range of luminosities ($L_\star$, $0.4L_\star$, and $4L_\star$) aimed at representing the cluster members from the faint ones to the BCG.

5. RESULTS

In this section we give the results of our visual cluster finding. During the inspection of each field, we classify each into four possible catalogs: High confidence, medium confidence, low confidence, and no detection. A high confidence result consists of a clear BCG and many accompanying satellite galaxies (see Figure **??**). A low confidence result is an ambiguous system where there is no clear BCG present but there appears to be a grouping of galaxies at a similar redshift. The medium confidence results fall in between the high and low confidence regimes where there appears to be a BCG but few satellite galaxies are observed. We fail to observe a cluster when there is no clear BCG candidate or clear group of galaxies at similar redshifts.

For the 112 fields observed with MOSAIC, we observe twelve high confidence clusters, twenty two both medium and low confidence clusters, and we observe no discernible cluster in sixty fields. In the following subsections we present on each of the eight high confidence observations individually, and group the medium and low confidence observations together.

5.1. *Observations of Known Clusters*

During the course of our observation campaign thirty clusters were confirmed through either dedicated follow up from the Planck team (e.g., Planck Collaboration et al. 2015, 2016) or through independent programs (e.g., Liu et al. 2015; van der Burg et al. 2016; Burenin 2017; Burenin et al. 2018; Amodeo et al. 2018; Barrena et al. 2018; Streblyanska et al. 2018). We can use this opportunity to validate our cluster detection method against known clusters. The thirty clusters are indicated in Table 2.

We successfully recovery XXX clusters. For the previously confirmed clusters which we cannot independently confirm, we discuss the potential reasons below.

5.1.1. *PSZ1 G031.91+67.94*

The position of the cluster reported in Planck Collaboration et al. (2016) is $\sim 18\farcm5$ from the reported PSZ1 position. We do not confirm a cluster within the $5'$ search radius used in our study.

5.1.2. *PSZ1 G084.62-15.86*

We recover a cluster at $z_{cl} = 0.271 \pm 0.099$ with 18 members. This is a system with at least three possible BCGs.

5.1.3. *PSZ1 G102.86-31.07*

We recover a cluster at $z_{cl} = 0.497 \pm 0.136$ with 13 possible members.

5.1.4. *PSZ1 G102.97-04.77*

Low galactic latitude make recovering any previously known cluster very difficult.

5.1.5. *PSZ1 G183.26+12.25*

Due to poor observing conditions, this field has a significantly lower limiting redshift give number. We are unable to confirm this cluster with $z = 0.85$.

5.1.6. *PSZ1 G206.45+13.89*

We find a cluster at $z_{cl} = 0.399 \pm 0.05$. We detect 73 potential cluster members, although a bright star (V = 4.5 mag; Høg et al. 2000) only $\sim 4\farcm9$ away from the reported BCG. The contaminating star prevents an accurate photo-z estimate for many cluster cluster members.

5.1.7. *PSZ2 G022.03+17.75*

PSZ2 G022.03+17.75 is previously reported as *PSZ1 G021.88+17.75* in Planck Collaboration et al. (2014). The position in the PSZ1 catalog differs signifcantly, give numbers from the position in the PSZ2 catalog. The position reported by Barrena et al. (2018) corresponds to the PSZ1 position. Because our study assumes the PSZ2 catalog replaces the corresponding entries in PSZ1 catalog, we cannot confirm a cluster within the search radius around the PSZ2 position.

5.1.8. *PSZ2 G033.27-17.54*

it looks like this BCG falls into the chipgap due to the observation strategy. I don't think we found this cluster because the BCG wasn't observed.

5.2. *Newly Discovered Clusters*

Lorem ipsum dolor amet swag copper mug meh tilde, put a bird on it live-edge tattooed kinfolk before they sold out locavore selvage leggings raclette literally bicycle rights. Hot chicken kickstarter mustache vinyl roof party. Wayfarers brooklyn truffaut twee umami, venmo irony. Typewriter viral pop-up, listicle vaporware organic af salvia keytar twee chillwave austin +1 offal blog. La croix dreamcatcher snackwave, try-hard intelligentsia taxidermy messenger bag air plant godard mustache celiac glossier echo park. Photo booth readymade authentic glossier biodiesel snackwave beard hammock sriracha before they sold out edison bulb fixie PBR&B. Man bun pabst kogi, crucifix subway tile af tacos cray tumeric lyft cronut lomo tattooed.

5.2.1. *PSZ1_G224.82+13.62*

previously confirmed

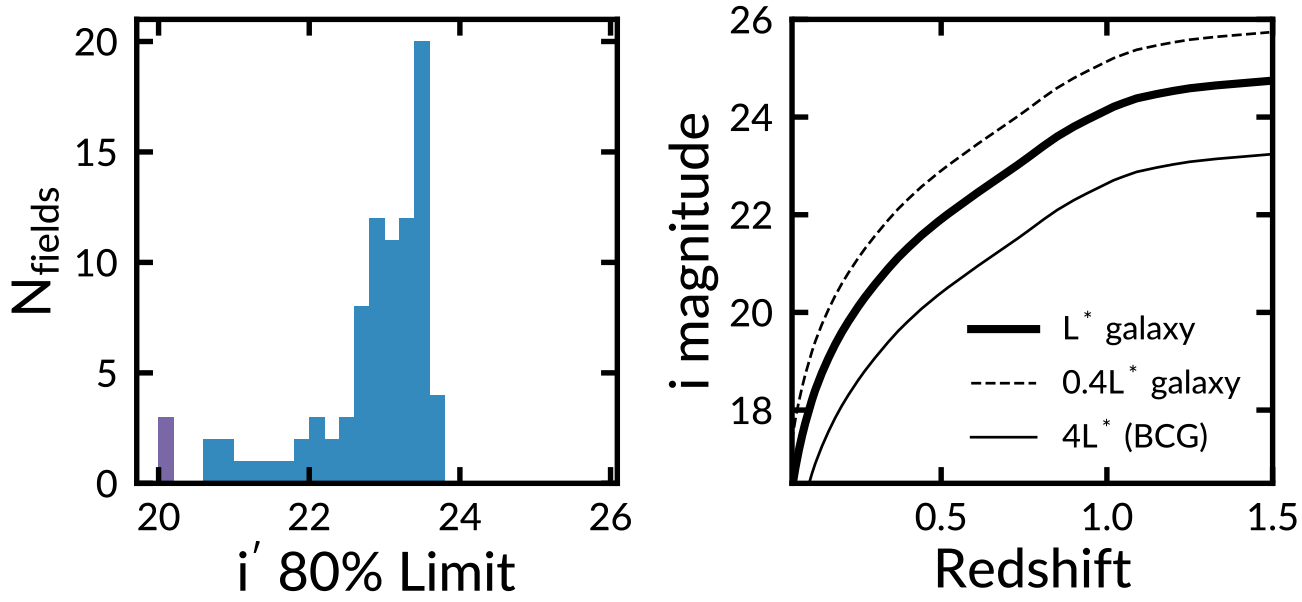

FIG. 2.— *Left:* Histogram of the *i*-band magnitude corresponding to 80% completeness in galaxy recovery. When 80% completeness is not achieved we show the limiting magnitude with the highest completeness. *Right:* Observed *i*-band magnitudes of $L_\star$, $0.4L_\star$, and $4L_\star$ (BCG) early-type galaxies as a function of redshift. We define an $L_\star$ galaxy following Blanton et al. (2003) as a population of red galaxies at $z = 0.1$ and allow it to evolve passively. The left and right panels can be combined to estimate the limiting redshift to which we could identify galaxy clusters.

TABLE 2
CAPTION

Name	RA PSZ	DEC PSZ	RA	DEC	Dist	z	Mag Lim	RA EX	DEC EX	Dist EX	z EX	Flag	Ref
PSZ1_G031.91+67.94	14:29:02	+24:37:33.38	NaN	NaN	NaN	NaN	23.20	14:30:23.299	+24:39:06.19	18.54	0.13	NaN	50.0
PSZ1_G055.83-41.64	21:57:14	-2:31:51	NaN	NaN	NaN	NaN	23.44	21:56:41.02	-02:32:20.87	8.25	0.63	3	-1.0
PSZ1_G084.62-15.86	21:49:44	+33:10:23.81	NaN	NaN	NaN	0.14	22.93	21:49:40.599	+33:10:34.59	0.73	0.37	NaN	50.0
PSZ1_G096.44-10.40	22:19:35	+44:31:05.27	NaN	NaN	NaN	NaN	22.80	22:20:12.95	+44:26:16.27	8.31	0.20	ND	-1.0
PSZ1_G102.86-31.07	23:33:08	+28:43:51.60	NaN	NaN	NaN	NaN	23.58	23:33:24.699	+28:43:19.89	3.70	0.59	NaN	50.0
PSZ1_G102.97-04.77	22:34:47	+52:43:13.90	NaN	NaN	NaN	NaN	21.56	22:34:47.08	+52:42:55.56	0.31	0.52	2	-1.0
PSZ1_G108.90-52.04	0:16:38	+09:52:49.98	NaN	NaN	NaN	NaN	23.48	00:16:26.74	+09:53:53.60	2.97	0.46	2	-1.0
PSZ1_G118.06+31.10	15:54:34	+84:10:37.49	NaN	NaN	NaN	NaN	22.69	15:54:38.699	+84:10:28.39	0.19	0.19	NaN	50.0
PSZ1_G138.60-10.85	2:27:02	+49:04:54.07	NaN	NaN	NaN	NaN	23.43	02:27:06.699	+49:00:29.29	4.48	0.70	NaN	50.0
PSZ1_G142.17+37.28	9:18:56	+70:52:01.14	NaN	NaN	NaN	NaN	23.30	09:19:05.16	+70:55:11.40	3.26	0.28	1	10.0
PSZ1_G142.38+22.82	6:13:40	+71:52:21.02	NaN	NaN	NaN	NaN	22.95	06:13:49.84	+71:52:54.78	0.95	0.39	2	-1.0
PSZ1_G146.00-49.42	1:51:35	+10:44:02.79	NaN	NaN	NaN	NaN	23.56	01:51:19.799	+10:47:29.99	5.09	0.10	NaN	50.0
PSZ1_G148.20+23.49	6:37:46	+66:54:24.40	NaN	NaN	NaN	NaN	23.21	06:37:54.60	+66:51:06.20	3.41	0.11	2	10.0
PSZ1_G153.41+36.58	8:42:40	+62:34:31.61	NaN	NaN	NaN	NaN	23.35	08:42:42.899	+62:30:21.59	4.18	0.65	NaN	50.0
PSZ1_G153.56+36.23	8:39:31	+62:31:30.58	NaN	NaN	NaN	NaN	23.27	08:39:33.399	+62:26:12.09	5.32	0.13	NaN	50.0
PSZ1_G162.30-26.92	3:24:26	+24:00:44.46	NaN	NaN	NaN	NaN	23.32	03:24:19.02	+23:57:49.82	3.32	0.39	2	-1.0
PSZ1_G169.80+26.10	7:30:08	+48:20:02.06	NaN	NaN	NaN	NaN	23.35	07:30:32.02	+48:17:39.05	4.65	0.73	2	-1.0
PSZ1_G183.26+12.25	6:42:56	+31:49:07.58	NaN	NaN	NaN	NaN	20.77	06:43:09.84	+31:50:55.47	3.45	0.85	2	500.0
PSZ1_G185.93-31.21	4:11:39	+06:16:00.67	NaN	NaN	NaN	NaN	22.71	04:11:52.31	+06:17:11.80	3.51	0.09	2	-1.0
PSZ1_G206.45+13.89	7:29:59	+11:56:22.64	NaN	NaN	NaN	NaN	20.00	07:29:51.23	+11:56:30.89	1.91	0.38	1	10.0
PSZ1_G224.82+13.62	8:01:42	-4:03:54	NaN	NaN	NaN	0.13	22.91	08:01:41.61	-04:03:46.23	0.16	0.29	1	10.0
PSZ1_G249.01+73.75	11:56:46	+16:55:43.68	NaN	NaN	NaN	NaN	23.08	11:57:05.599	+16:57:35.39	5.04	0.16	NaN	50.0
PSZ1_G286.25+62.68	12:21:10	+00:47:34.05	NaN	NaN	NaN	NaN	23.35	12:21:05.35	+00:48:22.29	1.41	0.21	3	-1.0
PSZ1_G341.69+50.66	14:25:20	-4:59:54	NaN	NaN	NaN	NaN	22.25	14:25:12.29	-04:56:34.19	3.84	0.30	1	10.0
PSZ2_G022.03+17.75	17:28:37	-1:13:03	NaN	NaN	NaN	NaN	23.17	17:28:16.01	-01:22:58.04	11.22	0.65	1	-1.0
PSZ2_G032.12-14.96	19:43:34	-7:27:45	NaN	NaN	NaN	NaN	22.51	19:43:11.20	-07:24:56.25	6.31	0.38	3	-1.0
PSZ2_G033.27-17.54	19:54:52	-7:36:11	NaN	NaN	NaN	NaN	22.64	19:54:59.67	-07:30:34.70	5.92	0.33	2	-1.0
PSZ2_G071.67-42.76	22:30:54	+05:42:05.22	NaN	NaN	NaN	NaN	23.56	22:30:50.00	+05:39:16.72	2.98	0.69	ND	-1.0
PSZ2_G093.04-32.38	23:01:43	+24:02:24.90	NaN	NaN	NaN	NaN	22.46	23:02:15.07	+24:03:50.50	7.46	0.51	3	-1.0
PSZ2_G310.81+83.91	12:55:01	+21:05:41.16	NaN	NaN	NaN	NaN	21.23	NaN	NaN	NaN	0.45	NaN	2.0

5.2.2. *PSZ2_G029.66-47.63*

5.2.3. *PSZ2_G043.44-41.27*

5.2.4. *PSZ2_G096.43-20.89*

5.2.5. *PSZ2_G106.11+24.11*

5.2.6. *PSZ2_G120.76+44.14*

5.2.7. *PSZ2_G173.76+22.92*

5.2.8. *PSZ2_G305.76+44.79*

5.3. *Redshift Limits in Other Fields*

Lorem ipsum dolor amet swag copper mug meh tilde, put a bird on it live-edge tattooed kinfolk before they sold out locavore selvage leggings raclette literally bicycle rights. Hot chicken kickstarter mustache vinyl roof party. Wayfarers brooklyn truffaut twee umami, venmo

irony. Typewriter viral pop-up, listicle vaporware organic af salvia keytar twee chillwave austin +1 offal blog. La croix dreamcatcher snackwave, try-hard intelligentsia taxidermy messenger bag air plant godard mustache celiac glossier echo park. Photo booth readymade authentic glossier biodiesel snackwave beard hammock sriracha before they sold out edison bulb fixie PBR&B. Man bun pabst kogi, crucifix subway tile af tacos cray tumeric lyft cronut lomo tattooed.

6. DISCUSSION

Lorem ipsum dolor amet swag copper mug meh tilde, put a bird on it live-edge tattooed kinfolk before they sold out locavore selvage leggings raclette literally bicycle rights. Hot chicken kickstarter mustache vinyl roof party. Wayfarers brooklyn truffaut twee umami, venmo irony. Typewriter viral pop-up, listicle vaporware organic af salvia keytar twee chillwave austin +1 offal blog. La croix dreamcatcher snackwave, try-hard intelligentsia taxidermy messenger bag air plant godard mustache celiac glossier echo park. Photo booth readymade authentic glossier biodiesel snackwave beard hammock sriracha before they sold out edison bulb fixie PBR&B. Man bun pabst kogi, crucifix subway tile af tacos cray tumeric lyft cronut lomo tattooed.

7. SUMMARY

Lorem ipsum dolor amet swag copper mug meh tilde, put a bird on it live-edge tattooed kinfolk before they sold out locavore selvage leggings raclette literally bicycle rights. Hot chicken kickstarter mustache vinyl roof party. Wayfarers brooklyn truffaut twee umami, venmo irony. Typewriter viral pop-up, listicle vaporware organic af salvia keytar twee chillwave austin +1 offal blog. La croix dreamcatcher snackwave, try-hard intelligentsia taxidermy messenger bag air plant godard mustache celiac glossier echo park. Photo booth readymade authentic glossier biodiesel snackwave beard hammock sriracha before they sold out edison bulb fixie PBR&B. Man bun pabst kogi, crucifix subway tile af tacos cray tumeric lyft cronut lomo tattooed.

ACKNOWLEDGEMENTS

This research made use of several open source packages: APLpy, an open-source plotting package for Python hosted at http://aplpy.github.com; the IPython package (Perez & Granger 2007); matplotlib, a Python library for publication quality graphics (Hunter 2007) and Astropy, a community developed core Python package for Astronomy (The Astropy Collaboration et al. 2013). IRAF is distributed by the National Optical Astronomy Observatory, which is operated by the Association of Universities for Research in Astronomy under cooperative agreement with the National Science Foundation (Tody 1993). PyRAF is a product of the Space Telescope Science Institute, which is operated by AURA for NASA. Funding for the SDSS and SDSS-II has been provided by the Alfred P. Sloan Foundation, the Participating Institutions, the National Science Foundation, the U.S. Department of Energy, the National Aeronautics and Space Administration, the Japanese Monbukagakusho, the Max Planck Society, and the Higher Education Funding Council for England. The SDSS Web Site is http://www.sdss.org/. The SDSS is managed by the Astrophysical Research Consortium for the Participating Institutions. This work has made use of data from the European Space Agency (ESA) mission *Gaia* (https://www.cosmos.esa.int/gaia), processed by the *Gaia* Data Processing and Analysis Consortium (DPAC, https://www.cosmos.esa.int/web/gaia/dpac/consortium). Funding for the DPAC has been provided by national institutions, in particular the institutions participating in the *Gaia* Multilateral Agreement. This research has made use of the VizieR catalogue access tool, CDS, Strasbourg, France. The original description of the VizieR service was published in Ochsenbein et al. (2000). This research has made use of the SVO Filter Profile Service (http://svo2.cab.inta-csic.es/theory/fps/) supported from the Spanish MINECO through grant AyA2014-55216.

REFERENCES

Alam, S., Albareti, F. D., Prieto, C. A., et al. 2015, The Astrophysical Journal Supplement Series, 219, 12
Amodeo, S., Mei, S., Stanford, S. A., et al. 2018, The Astrophysical Journal, 853, 36
Barrena, R., Streblyanska, A., Ferragamo, A., et al. 2018, eprint arXiv:1803.05764, arXiv:1803.05764
Benitez, N. 2000, The Astrophysical Journal, 536, 571
Bertin, E. 2006, in Astronomical Society of the Pacific Conference Series, Vol. 351, Astronomical Data Analysis Software and Systems XV, ed. C. Gabriel, C. Arviset, D. Ponz, & S. Enrique, 112
Bertin, E., & Arnouts, S. 1996, Astronomy and Astrophysics Supplement Series, 117, 393
Bertin, E., & Emmanuel. 2011, Astrophysics Source Code Library, record ascl:1110.006
Bertin, E., Mellier, Y., Radovich, M., et al. 2002, in Astronomical Society of the Pacific Conference Series, Vol. 281, Astronomical Data Analysis Software and Systems XI, ed. D. Bohlender, D. Durand, & T. Handley, 228
Blanton, M. R., Hogg, D. W., Bahcall, N. A., et al. 2003, The Astrophysical Journal, 592, 819
Bruzual, G., & Charlot, S. 2003, Monthly Notices of the Royal Astronomical Society, 344, 1000
Burenin, R. A. 2017, Astronomy Letters, 43, 507
Burenin, R. A., Bikmaev, I. F., Khamitov, I. M., et al. 2018, eprint arXiv:1801.04464, arXiv:1801.04464
Carlstrom, J. E., Ade, P. A. R., Aird, K. A., et al. 2011, Publications of the Astronomical Society of the Pacific, 123, 568
Chabrier, G. 2003, Publications of the Astronomical Society of the Pacific, 115, 763
Chambers, K. C., Magnier, E. A., Metcalfe, N., et al. 2016, eprint arXiv:1612.05560, arXiv:1612.05560
Coe, D., Benitez, N., Sanchez, S. F., et al. 2006, The Astronomical Journal, 132, 926
Dahlen, T., Mobasher, B., Faber, S. M., et al. 2013, The Astrophysical Journal, 775, 93
de Vaucouleurs, G. 1948, Annales d'Astrophysique, 11, 247
Flewelling, H. A., Magnier, E. A., Chambers, K. C., et al. 2016, eprint arXiv:1612.05243, arXiv:1612.05243
Foley, R. J., Andersson, K., Bazin, G., et al. 2011, The Astrophysical Journal, 731, 86
Gaia Collaboration, G., Brown, A. G. A., Vallenari, A., et al. 2016a, Astronomy & Astrophysics, Volume 595, id.A2, 23 pp., 595, arXiv:1609.04172
Gaia Collaboration, G., Prusti, T., de Bruijne, J. H. J., et al. 2016b, Astronomy & Astrophysics, Volume 595, id.A1, 36 pp., 595, arXiv:1609.04153
Høg, E., Fabricius, C., Makarov, V. V., et al. 2000, Astronomy and Astrophysics, 355, L27
Hunter, J. D. 2007, Computing in Science & Engineering, 9, 90
Ilbert, O., Capak, P., Salvato, M., et al. 2009, The Astrophysical Journal, 690, 1236
Jenkins, A., Frenk, C. S., White, S. D. M., et al. 2001, Monthly Notices of the Royal Astronomical Society, 321, 372
Komatsu, E., Smith, K. M., Dunkley, J., et al. 2011, The Astrophysical Journal Supplement Series, 192, 18

Liu, J., Hennig, C., Desai, S., et al. 2015, Monthly Notices of the Royal Astronomical Society, 449, 3370
Menanteau, F., Hughes, J. P., Jimenez, R., et al. 2009, The Astrophysical Journal, 698, 1221
Menanteau, F., Hughes, J. P., Barrientos, L. F., et al. 2010a, The Astrophysical Journal Supplement Series, 191, 340
Menanteau, F., González, J., Juin, J.-B., et al. 2010b, The Astrophysical Journal, 723, 1523
Menanteau, F., Hughes, J. P., Sif?n, C., et al. 2012, The Astrophysical Journal, 748, 7
Molino, A., Benítez, N., Ascaso, B., et al. 2017, Monthly Notices of the Royal Astronomical Society, 470, 95
Mommert, M., & M. 2017, Astronomy and Computing, 18, 47
Ochsenbein, F., Bauer, P., & Marcout, J. 2000, Astronomy and Astrophysics Supplement Series, 143, 23
Oke, J. B. 1974, The Astrophysical Journal Supplement Series, 27, 21
Perez, F., & Granger, B. E. 2007, Computing in Science & Engineering, 9, 21
Planck Collaboration, Ade, P. A. R., Aghanim, N., et al. 2014, Astronomy & Astrophysics, 571, A29
—. 2015, Astronomy & Astrophysics, 582, A29
—. 2016, Astronomy & Astrophysics, 586, A139
Streblyanska, A., Barrena, R., Rubino-Martin, J. A., et al. 2018, eprint arXiv:1804.01356, arXiv:1804.01356
Sunyaev, R. A., & Zeldovich, Y. B. 1972, Comments on Astrophysics and Space Physics, 4
Swetz, D. S., Ade, P. A. R., Amiri, M., et al. 2011, The Astrophysical Journal Supplement Series, 194, 41
The Astropy Collaboration, Robitaille, T. P., Tollerud, E. J., et al. 2013, Astronomy & Astrophysics, 558, A33
Tinker, J., Kravtsov, A. V., Klypin, A., et al. 2008, The Astrophysical Journal, 688, 709
Tody, D. 1993, Astronomical Data Analysis Software and Systems II, 52
Valdes, F. G., & Swaters, R. A. 2007, in Astronomical Society of the Pacific Conference Series, Vol. 376, Astronomical Data Analysis Software and Systems XVI, ed. R. Shaw, F. Hill, & D. Bell, 273
van der Burg, R. F. J., Aussel, H., Pratt, G. W., et al. 2016, Astronomy & Astrophysics, 587, A23
York, D. G., Adelman, J., Anderson, John E., J., et al. 2000, The Astronomical Journal, 120, 1579